

# Revealing quantum Hall states in epitaxial topological half-Heusler semimetal

Shouvik Chatterjee,<sup>1,2,\*</sup> Felipe Crasto de Lima,<sup>3,4</sup> John A. Logan,<sup>5</sup> Yuan Fang,<sup>6</sup> Hadass Inbar,<sup>5</sup> Aranya Goswami,<sup>1</sup> Connor Dempsey,<sup>1</sup> Shoaib Khalid,<sup>7,3</sup> Tobias Brown-Heft,<sup>5</sup> Yu-Hao Chang,<sup>5</sup> Taozhi Guo,<sup>8</sup> Daniel Pennacchio,<sup>5</sup> Nathaniel Wilson,<sup>5</sup> Jason Dong,<sup>5</sup> Shalinee Chikara,<sup>9</sup> Alexey Suslov,<sup>9</sup> Alexei V. Fedorov,<sup>10</sup> Dan Read,<sup>1,11</sup> Jennifer Cano,<sup>6,12</sup> Anderson Janotti,<sup>3</sup> and Christopher J. Palmström<sup>1,5,13,\*</sup>

<sup>1</sup>*Department of Electrical and Computer Engineering,  
University of California, Santa Barbara, CA 93106, USA*

<sup>2</sup>*Department of Condensed Matter Physics and Materials Science,  
Tata Institute of Fundamental Research, Homi Bhabha Road, Mumbai 400005, India*

<sup>3</sup>*Department of Materials Science and Engineering,  
University of Delaware, Newark, DE 19716, USA*

<sup>4</sup>*Instituto de Física, Universidade Federal de Uberlândia, C.P. 593, 38400-592, Uberlândia, MG, Brazil*

<sup>5</sup>*Materials Department, University of California, Santa Barbara, CA 93106, USA*

<sup>6</sup>*Department of Physics and Astronomy, Stony Brook University, Stony Brook, New York, 11974, USA*

<sup>7</sup>*Department of Physics and Astronomy, University of Delaware, Newark, DE 19716, USA*

<sup>8</sup>*Department of Physics, University of California, Santa Barbara, CA 93106, USA*

<sup>9</sup>*National High Magnetic Field Laboratory, Tallahassee, FL 32310, USA*

<sup>10</sup>*Advanced Light Source, Lawrence Berkeley National Laboratory, Berkeley, CA 94720, USA*

<sup>11</sup>*School of Physics and Astronomy, Cardiff University, Cardiff CF24 3AA, UK*

<sup>12</sup>*Center for Computational Quantum Physics, Flatiron Institute, New York, New York, 10010, USA*

<sup>13</sup>*California NanoSystems Institute, University of California, Santa Barbara, California 93106, USA*

**Prediction of topological surface states (TSS) in half-Heusler compounds raises exciting possibilities to realize exotic electronic states and novel devices by exploiting their multifunctional nature. However, an important prerequisite is identification of macroscopic physical observables of the TSS, which has been difficult in these semimetallic systems due to prohibitively large number of bulk carriers. Here, we introduce compensation alloying in epitaxial thin films as an effective route to tune the chemical potential and simultaneously reduce the bulk carrier concentration by more than two orders of magnitude compared to the parent compound. Linear magnetoresistance is shown to appear as a precursor phase that transmutes into a TSS induced quantum Hall phase on further reduction of the coupling between the surface states and the bulk carriers. Our approach paves the way to reveal and manipulate exotic properties of topological phases in Heusler compounds.**

Heusler compounds are a class of inter-metallic systems that exhibit a wide range of electrical and magnetic properties [1–3] including materials that are semiconductors [4], half-metallic ferromagnets [5], thermoelectrics [6], and superconductors [7, 8]. They have also been predicted to host exotic topological phases [9, 10]. PtLuSb is one such compound, where a band inversion between the  $\Gamma_8$  (p-type character) and the  $\Gamma_6$  (s-type character) manifolds results in its topologically non-trivial character.

In such cases, bulk-boundary correspondence guarantees the existence of strongly spin-orbit coupled surface states that have been observed in recent angle-resolved photoemission spectroscopy (ARPES) measurements [11]. However, the presence of a large number of bulk carriers due to the semimetallic nature of these compounds and strong coupling between the bulk and the surface states have precluded the identification of macroscopic physical observables of the topological surface states (TSS) in any Heusler compound. Intrinsic doping in these compounds, ascribed to the presence of anti-site defects [12], further exacerbates the problem. In PtLuSb, this results in the chemical potential to lie deep inside the valence band away from the quadratic band touching point ( $\Gamma_8$ ) at the top of the bulk valence band, where the chemical potential is predicted to lie in density functional theory (DFT) calculations (Fig. 1d)[11, 13]. The inability to disentangle the contribution of the TSS from the bulk carriers imposes serious constraints on the utility of these compounds in device applications and in the realization of exotic phases of matter by exploiting their multi-functional nature.

To control the chemical potential and decouple the surface states from the bulk carriers we have synthesized epitaxial thin films of Pt<sub>1-x</sub>Au<sub>x</sub>LuSb with different gold compositions, where gold (Au) atoms are expected to contribute one extra electron per formula unit compared to platinum (Pt). This has allowed us not only to tune the surface chemical potential close to the Dirac point, but also to lower the bulk carrier concentration by more than two orders of magnitude. Reduction of both concentration of the bulk carriers and their coupling to the surface states in substitutionally alloyed Pt<sub>1-x</sub>Au<sub>x</sub>LuSb thin films combined with a lower effective mass of the TSS has led to the observation of quantum Hall states.

\*Authors to whom correspondence should be addressed: shouvik.chatterjee@tifr.res.in, cjpalm@ucsb.edu

In addition, our ability to continuously tune the bulk carrier concentration and surface-bulk coupling in the same material system allowed us to reveal the connection between the appearance of non-saturating linear magnetoresistance and the presence of linearly dispersive TSS, showing how well defined quantum Hall states emerge from such a magnetoresistance behaviour when the coupling between the surface states and bulk carriers is reduced.

Epitaxial thin films of 15 nm thick  $\text{Pt}_{1-x}\text{Au}_x\text{LuSb}$  were synthesized on InSb buffer layers on GaAs(001) substrates. Details of the growth process and film characterization can be found in the methods section and in the Supplementary Information [14]. The addition of gold (Au) is found to have a dramatic effect on the charge transport in  $\text{Pt}_{1-x}\text{Au}_x\text{LuSb}$  thin films. Magnetoresistance ( $\Delta\rho_{xx}(B)/\rho_{xx}(0)$ ) in substitutionally alloyed thin films increases by more than two orders of magnitude compared to PtLuSb, as shown in Fig. 1a. While magnetoresistance starts to saturate at higher magnetic fields for higher gold concentrations ( $x = 3/8, 1/2$ ), remarkably linear magnetoresistance behavior is observed to persist in thin films with lower Au concentrations ( $x = 1/8, 1/4$ ). Carrier concentration, as estimated from low-field Hall measurements, drops from  $3.53 \times 10^{20} \text{ cm}^{-3}$  in PtLuSb to  $7.53 \times 10^{17} \text{ cm}^{-3}$  in  $\text{Pt}_{7/8}\text{Au}_{1/8}\text{LuSb}$ , a change by almost three orders of magnitude on the addition of gold. Low field Hall measurements also indicate a change in the carrier type from predominantly p-type to n-type in gold alloyed samples. The bulk band structure obtained from DFT calculations coupled with the carrier concentration estimated from the low-field Hall measurements indicates that the Fermi level lies very close to the four-fold degenerate  $\Gamma_8$  point in the gold doped samples, as shown in Fig 1d.

In addition to donating one extra electron per formula unit the addition of gold is expected to maintain the band inversion similar to what has been predicted for the parent compound [14], thus providing a pathway to tune the occupation of the topological surface states. In our experiment, the changes in the electronic structure due to compensation alloying of gold in  $\text{Pt}_{1-x}\text{Au}_x\text{LuSb}$  is directly observed in the ARPES measurements. In Fig. 2 we show the ARPES data taken along  $\bar{\Gamma} - \bar{X}$  of the surface Brillouin zone (see Fig. S7 in Supplementary Information [14]) close to the bulk  $\Gamma$  point for three different gold concentrations in  $\text{Pt}_{1-x}\text{Au}_x\text{LuSb}$  with  $x = 0, 1/8, \text{ and } 3/8$ . For the parent compound PtLuSb, the extracted dispersion of the topological surface state (TSS), shown in Fig. 2e, is identical to what has been observed in our previous work, where spin-momentum locking of the surface state was revealed by spin-resolved ARPES [11]. This confirms that we are measuring the same TSS in our current set of samples. Two-dimensional nature of the TSS is established by photon energy dependent measurements shown in Fig. S8 in the Supplementary Information [14]. On the addition of gold, the chemical potential is shifted to higher energies but the dispersion

of the TSS remains unchanged. The measured Fermi velocity of the TSS is  $v_F = 4.85 \times 10^5 \text{ m/s}$ , which is in close agreement with the predicted  $v_F = 4.9 \pm 0.3 \times 10^5 \text{ m/s}$  in the DFT slab calculations (see Supplementary Information [14]). From the extracted dispersion of the TSS we estimate the shift in the surface chemical potential due to addition of Au to be 180 meV and 330 meV for  $\text{Pt}_{7/8}\text{Au}_{1/8}\text{LuSb}$  and  $\text{Pt}_{5/8}\text{Au}_{3/8}\text{LuSb}$ , respectively, shown in Fig. 2d. However, an energy gap in the TSS is observed in the ARPES spectra for  $\text{Pt}_{5/8}\text{Au}_{3/8}\text{LuSb}$  (Fig. 2c) indicative of the formation of massive Dirac fermions due to coupling between the TSS at opposite surfaces of  $\text{Pt}_{1-x}\text{Au}_x\text{LuSb}$  thin films (see also Fig. S7 in the Supplementary Information[14]). The wavefunctions of TSS at opposite surfaces overlap to open a bandgap in thin films with thicknesses less than the critical thickness,  $\xi_c$  given by  $\xi_c = 2\hbar v_F/\Delta$ , where  $\Delta$  is the charge excitation gap and  $\xi$  is the surface penetration depth [15]. We estimate a bulk band gap of 18.72 meV in our 15 nm thick films due to quantum confinement from the  $k \cdot p$  fitting of the bulk band structure calculated from DFT [14]. This results in a critical thickness  $\xi_c \approx 34 \text{ nm}$ , much larger than the thickness of our thin films indicating a significant overlap between the TSS wavefunctions at the opposite surfaces, in agreement with our ARPES data. A comparison between the Fermi levels obtained from the ARPES (surface) and Hall measurements (bulk) indicates an upward band-bending near the sample surface, typically observed in semiconductors where the Fermi level is pinned at the surface [16], as shown schematically in Fig. 2e. While the band-bending is negligible (3 meV) in PtLuSb, a steep band-bending of 225 meV and 123 meV is observed for  $\text{Pt}_{7/8}\text{Au}_{1/8}\text{LuSb}$  and  $\text{Pt}_{5/8}\text{Au}_{3/8}\text{LuSb}$ , respectively. Details about the estimation of band-bending can be found in the Supplementary Information [14]. The observed trend is likely due to the enhanced surface defects that act as negatively charged acceptors and low bulk carrier concentration in the gold doped samples. The presence of bulk bands that cross the Fermi level at the surface in addition to the TSS is expected to result in a short screening length.

To understand the evolution of the transport properties with the addition of Au in  $\text{Pt}_{1-x}\text{Au}_x\text{LuSb}$  we compare magnetotransport data from  $\text{Pt}_{7/8}\text{Au}_{1/8}\text{LuSb}$  and  $\text{Pt}_{5/8}\text{Au}_{3/8}\text{LuSb}$  samples, which show surprisingly contrasting behavior. Remarkably linear non-saturating magnetoresistance is observed in  $\text{Pt}_{7/8}\text{Au}_{1/8}\text{LuSb}$  up to a magnetic field of  $\approx 22\text{T}$ , above which it begins to deviate. In contrast, magnetoresistance in  $\text{Pt}_{5/8}\text{Au}_{3/8}\text{LuSb}$  appears to saturate with a sub-linear magnetic field dependence from where quantum Hall states emerge for magnetic field values greater than  $\approx 10\text{T}$ . Though the magnetoresistance behavior in  $\text{Pt}_{1-x}\text{Au}_x\text{LuSb}$  films with different Au concentration appears very different, that they share a common underlying origin is established from their respective magnetoconductance plots  $G_{xx/xy} = \frac{R_{xx/xy}}{R_{xx}^2 + R_{xy}^2}$ , shown in Fig. 3c,d. In both the films, quantum Hall plateaus begin to appear in  $G_{xy}$  above  $\approx 10\text{T}$ ,

Table I: Model parameters

Parameters	Pt <sub>7/8</sub> Au <sub>1/8</sub> LuSb	Pt <sub>5/8</sub> Au <sub>3/8</sub> LuSb
$\mu$ (meV)	126	116
$g$	7.5	10.3
$\Delta_h$ (meV)	66	51
$\Delta_i$ (meV)	3	2
$k_F$ ( $\text{\AA}^{-1}$ )	0.034	0.033

which is ascribed to the presence of two-dimensional TSS shown in our ARPES measurements. However, the corresponding local maxima in magnetoconductance  $G_{xx}$  is better resolved in Pt<sub>5/8</sub>Au<sub>3/8</sub>LuSb indicative of a reduced surface-bulk coupling, which is manifested in the observation of well-resolved quantum Hall plateaus in the resistance data (see Fig. 3b). At extremely high magnetic field values of  $\approx 45$ T, surface-bulk coupling is sufficiently reduced in Pt<sub>7/8</sub>Au<sub>1/8</sub>LuSb as well, which results in the appearance of a local minimum in magnetoresistance emerging out of the linear magnetoresistance behavior, similar to what is observed for Pt<sub>5/8</sub>Au<sub>3/8</sub>LuSb. The appearance of local minima in magnetoresistance instead of local maxima, generally observed in traditional quantum Hall measurements, can be understood by noting that in contrast to the traditional quantum Hall systems,  $R_{xy} \ll R_{xx}$  in our thin films that leads to an additional negative sign when converting to resistance using the conductance tensor [17]. The local minima in magnetoresistance indeed correspond to local maxima in magnetoconductance, as shown in Figs. 3e,f. Further evidence for an enhanced surface-bulk coupling in Pt<sub>7/8</sub>Au<sub>1/8</sub>LuSb compared to Pt<sub>5/8</sub>Au<sub>3/8</sub>LuSb is obtained from an analysis of their weak anti-localization (WAL) behavior [14]. Our measurements establish that the linear magnetoresistance behavior in topological semimetals can be understood as a precursor phase from where the quantum Hall phenomenon can emerge on further reduction of the surface-bulk coupling.

Having described the magnetotransport properties in our thin films we construct a simple model to understand how quantum Hall states emerge from the TSS in the semi-metallic thin films. We assume the presence of linearly dispersive TSS at both the surfaces of our thin films given by

$$H_{TSS} = \hbar v_f (k_x \sigma_y - k_y \sigma_x) \otimes \tau_z \quad (1)$$

where the film surface vector is along the  $z$  axis,  $\sigma_i$  ( $\tau_i$ ) represents the spin (surface) subspace. We further add a Zeeman term ( $H_Z$ ), a hybridization term ( $H_{hyb}$ ) that captures the interaction between the two TSS at opposite surfaces leading to the opening of a hybridization gap as observed in the ARPES measurements, and an inversion symmetry breaking term ( $H_{invb}$ ) that lifts the degeneracy between the TSS at opposite surfaces, which could arise due to different screening effect and/or different surface

potential at the two surfaces. The total Hamiltonian is

$$H_{tot} = H_{TSS} + H_Z + H_{hyb} + H_{invb} \quad (2)$$

where

$$H_Z = g \mu_B B_0 \sigma_z \otimes \mathbb{1} \quad (3)$$

$$H_{hyb} = \Delta_h \mathbb{1} \otimes \tau_x \quad (4)$$

$$H_{invb} = \Delta_i \mathbb{1} \otimes \tau_z \quad (5)$$

Note that the  $g$ -factor is the effective  $g$ -factor that incorporates orbital contributions of the bulk bands, thus capturing the modification of the surface state dispersion from the ideal Dirac-like behavior. Evidence for  $g$ -factor anisotropy in the surface states is obtained from the angle-dependent magnetoresistance measurements [14]. From the equations above we obtain the Landau energy levels given by

$$\mu = \left[ 2v_F^2 n e \hbar B_0 + (g \mu_B B_0)^2 + \Delta_h^2 + \Delta_i^2 \right. \\ \left. \pm 2 \sqrt{(g \mu_B B_0 \Delta_i)^2 + (g \mu_B B_0 \Delta_h)^2 + 2v_F^2 n e \hbar B_0 \Delta_i^2} \right]^{1/2} \quad (6)$$

In Fig. 4 we plot the calculated density of states from the above model, which describes the quantum Hall behavior in our thin films very well. Inclusion of a finite  $g$ -factor and a hybridization gap of the TSS was found to be essential to model our data in agreement with the observation of a finite gap in TSS in the ARPES data. Extracted parameters from the model are summarised in Table 1. Similar chemical potential values are obtained for Pt<sub>7/8</sub>Au<sub>1/8</sub>LuSb and Pt<sub>5/8</sub>Au<sub>3/8</sub>LuSb at high magnetic fields (Table 1), which, however, differs significantly from the zero-field values obtained from the ARPES measurements (Fig. 2, see  $\Delta_3$  values in Table S1 in the Supplementary Information [14]). In addition, the chemical potential values in Pt<sub>7/8</sub>Au<sub>1/8</sub>LuSb, which has the lowest bulk carrier concentration, is found to be quite close at both zero and high magnetic fields. Such a behavior can be understood by noting that the quantum Hall states appear in Pt<sub>1-x</sub>Au<sub>x</sub>LuSb after they are in the bulk quantum limit [14], which results in a similar band-bending behavior at high magnetic fields for different gold concentrations, but can differ at low fields due to different bulk screening effect.

To rule out the possible bulk origin of the observed quantum Hall effect we explicitly calculated the Landau levels taking into account both the orbital and Zeeman effects along with quantum confinement due to the finite thickness of our thin films. We utilized a  $k.p$  fitting of the bulk-band structure along with the estimated Fermi levels from the low-field Hall coefficient (Fig. 1d) for the calculations, details of which can be found in the Supplementary Information [14]. Even after the inclusion of a range of plausible  $g$ -factor values for the bulk bands, the experimental data cannot be reconciled with the estimated Landau levels ruling out the possibility of their bulk origin. Another possible origin of the ob-

served quantum Hall behavior is the presence of massive, doubly degenerate Volkov-Pankratov states at the  $\text{Pt}_{1-x}\text{Au}_x\text{LuSb} / \text{InSb}$  hetero-interface [18–20]. However, such states can only arise for a smooth hetero-interface where the gap evolves over a length  $l$  greater than  $\xi$ , which is impossible in our case as the estimated value of  $\xi$  in  $\text{Pt}_{1-x}\text{Au}_x\text{LuSb}$  thin films exceeds the film thickness. Another tantalizing possibility for the origin of the observed quantum Hall effect could be the Fermi arc states [21] that originate from magnetic field induced Weyl points, as has been predicted in the half-Heusler compounds [22]. However, symmetry constraints on the Fermi arc states explicitly rule out the possibility of lifting the degeneracy of the Fermi arc induced quantum Hall states under a magnetic field, in contrast to our experimental observation [14].

In summary, our work has unambiguously revealed the macroscopic physical observables of the TSS in a semi-metallic half-Heusler compound  $\text{Pt}_{1-x}\text{Au}_x\text{LuSb}$ , thus establishing its topological nature. We have also experimentally established the appearance of linear magnetoresistance as a precursor phase for the quantum Hall behavior and its connection to the presence of TSS by continuously tuning the surface-bulk coupling within the same material system. Our work establishes compensation alloying as a useful strategy to both reveal and exploit exotic properties in semi-metallic systems.

### Acknowledgments

We thank Mihir Pendharkar for helpful discussions. Synthesis of thin films, development of the UHV suitcase, ARPES experiments, and theoretical work were supported by the US Department of Energy (Contract no. DE-SC0014388). Development of the growth facilities and low temperature magnetotransport measurements were supported by the Office of Naval Research through the Vannevar Bush Faculty Fellowship under the Award No. N00014-15-1-2845. Scanning probe studies were supported by National Science Foundation (Award number DMR-1507875). This research used resources of the Advanced Light Source, which is a DOE Office of Science User Facility under contract no. DE-AC02-05CH11231. A portion of this work was performed at the National High Magnetic Field Laboratory, which is supported by the National Science Foundation Cooperative Agreement DMR-1644779 and the state of Florida. We acknowledge the use of shared facilities of the National Science Foundation (NSF) Materials Research Science and Engineering Center (MRSEC) (DMR 1720256) at the University of California Santa Barbara, the UCSB Nanofabrication Facility, an open access laboratory, and the LeRoy Eyring Center for Solid State Science at Arizona State University. Density functional theory calculations made use of the National Energy Research Scientific Computing Center (NERSC), a U.S. Department of Energy Office of Science User Facility operated under Contract no. DE-

AC02-05CH11231. Theoretical analysis (J.C. and Y.F.) was supported by the National Science Foundation under Grant No. DMR-1942447. J.C. acknowledges the support of the Flatiron Institute, a division of the Simons Foundation. D.R. gratefully acknowledges support from the Leverhulme Trust via an International Academic Fellowship (IAF-2018-039).

### Author contribution

S.C., J.A.L., and C.J.P. conceived the study. Thin film growth was performed by S.C. and J.A.L. Device fabrication and transport measurements were performed by S.C. with the assistance from D.R., A.G., C.D., H.I., Sha.C., and A.S. ARPES measurements were performed and analyzed by S.C. with the assistance from H.I., T.B., Y.C., D.R., and A.F. STM measurements were performed by N.W. and J.D. TEM measurements were performed by D.P. and A.G. DFT calculations were performed by F.C.L. and S.K. under the supervision of A.J. Theoretical analyses were performed by Y.F., S.C., and J.C. The manuscript was prepared by S.C. and C.J.P. All authors discussed results and commented on the manuscript.

### Methods

#### A. Thin Film Growth

Epitaxial thin films of 15 nm thick  $\text{Pt}_{1-x}\text{Au}_x\text{LuSb}$  were synthesized on a 270 nm thick InSb buffer layer grown on GaAs substrates by molecular-beam epitaxy (MBE). InSb atomic layers were nucleated at 360°C and grown at 410°C following thermal desorption of the native oxide on GaAs substrates. During the growth process, InSb (6.479 Å) atomic layers were almost immediately relaxed due to a large lattice mismatch with GaAs (5.653 Å). InSb buffer layers, which are grown in a modified VG-80 MBE system were taken out of the chamber post-growth and loaded into a modified Veeco Gen-II MBE system where the surface oxide was removed by atomic hydrogen before the growth of  $\text{Pt}_{1-x}\text{Au}_x\text{LuSb}$  atomic layers.  $\text{Pt}_{1-x}\text{Au}_x\text{LuSb}$ , which has a lattice constant similar to that of InSb grows as a pseudomorphic epitaxial layer with respect to the underlying InSb buffer layer.  $\text{Pt}_{1-x}\text{Au}_x\text{LuSb}$  thin films of different gold concentrations were all grown on the same InSb buffer layer, which was cleaved outside the vacuum chamber into smaller pieces for individual  $\text{Pt}_{1-x}\text{Au}_x\text{LuSb}$  growths.  $\text{PtLuSb}$  thin films were grown at substrate temperatures between 370°C and 400°C. Substrate temperatures were progressively lowered for thin-film growths with higher gold concentration with the  $\text{Pt}_{1/2}\text{Au}_{1/2}\text{LuSb}$  thin films grown at the substrate temperatures between 310°C and 340°C. For  $\text{Pt}_{1-x}\text{Au}_x\text{LuSb}$  growths Lu, Au, and Sb were evaporated from effusion cells, while Pt was evaporated using an e-beam evaporator. Atomic fluxes of

Lu, Au, Sb, and Pt were calibrated by Rutherford back-scattering spectrometry (RBS) measurements of the elemental areal atomic density of calibration samples grown on Si substrates. These measurements were then used to calibrate *in-situ* beam flux measurements using an ion gauge for Lu, Au, Sb, and a quartz crystal microbalance (QCM) for Pt.

## B. ARPES

ARPES measurements were performed at the Advanced Light Source at the end station 10.0.1.2. Samples were transferred from the growth chamber at UCSB to an analysis chamber equipped with a Scienta R4000 spectrometer at ALS in a custom-built UHV suitcase allowing us to maintain the pristine sample surface throughout the entire sample transfer process. Samples were cooled to a temperature of 70K with liquid nitrogen. Tunable synchrotron light with photon energies in the range of 20 - 80 eV was used for the measurements.

## C. Transport Measurements

Transport measurements were performed on fabricated Hall bar devices using standard low frequency a.c. lock-in technique. Measurements were performed in-house using a Quantum Design PPMS equipped with a 14 Tesla mag-

net and at the National High Magnetic Field Lab at Tallahassee, Florida using a 35 Tesla and a hybrid 45 Tesla magnets. Hall bars of dimension  $400\ \mu\text{m} \times 100\ \mu\text{m}$  were fabricated using standard optical lithography followed by an ion milling procedure using argon ions. Contacts were made using  $50\ \mu\text{m}$  gold wires bonded onto lithographically patterned gold contacts. A low current of  $1\ \mu\text{A}$  was sourced for all measurements to avoid Joule heating with the current flowing along the [110] crystallographic axis unless mentioned otherwise.

## D. DFT Calculations

The calculations were performed based on the DFT approach, as implemented in the VASP code [23]. The exchange-correlation term was described using the GGA functional proposed by Perdew, Burke, and Ernzerhof [24]. The Kohn-Sham orbitals are expanded in a plane wave basis set with an energy cutoff of 400 eV. The Brillouin zone is sampled according to the Monkhorst-Pack method [25], using a gamma-centered  $7 \times 7 \times 5$  ( $7 \times 7 \times 1$ ) mesh for the tetragonal bulk (slab) calculations. The electron-ion interactions are taken into account using the Projector Augmented Wave method [26]. All geometries have been relaxed until atomic forces were lower than  $0.01\ \text{eV}/\text{\AA}$ . For the slab calculations, to avoid significant interaction between periodic images, a vacuum region of  $15\ \text{\AA}$  was considered.

- 
- [1] Wollmann, L., Nayak, A. K., Parkin, S. S. P., Felser, C. Heusler 4.0: tunable materials. *Annu. Rev. Mater. Res.* **47**, 247-270 (2017).
  - [2] Graf, T., Felser, C., Parkin, S. S. P. Simple rules for the understanding of Heusler compounds. *Prog. Solid State Ch.* **39**, 1-50 (2011).
  - [3] Palmström, C. J. Heusler compounds and spintronics. *Prog. Cryst. Growth Charact. Mater.* **62**, 371-397 (2016).
  - [4] Kawasaki, J. K., Johansson, L. I. M., Schultz, B. D., Palmström, C. J. Growth and transport properties of epitaxial lattice matched half-Heusler CoTiSb/InAlAs/InP (001) heterostructures. *Appl. Phys. Lett.* **104**, 022109 (2014).
  - [5] De Groot, R. A., Mueller, F. M., Van Engen, P. G., Buschow, K. H. J. New class of materials: half-metallic ferromagnets. *Phys. Rev. Lett.* **50**, 2024 (1983).
  - [6] Hinterleitner, B., et al. Thermoelectric performance of a metastable thin-film Heusler alloy. *Nature* **576**, 85-90 (2019).
  - [7] Klimczuk, T., et al. Superconductivity in the Heusler family of intermetallics. *Phys. Rev. B* **85**, 174505 (2012).
  - [8] Nakajima, Y., et al. Topological RPdBi half-Heusler semimetals: A new family of non-centrosymmetric magnetic superconductors. *Sci. Adv.* **1**, e1500242 (2015).
  - [9] Chadov, S., et al. Tunable multifunctional topological insulators in ternary Heusler compounds. *Nat. Mater.* **9**, 541-545 (2010).
  - [10] Lin, H., et al. Half-Heusler ternary compounds as new multifunctional experimental platforms for topological quantum phenomena. *Nat. Mater.* **9**, 546-549 (2010).
  - [11] Logan, J. A., et al. Observation of a topologically non-trivial surface state in half-Heusler PtLuSb (001) thin films. *Nat. Commun.* **7**, 1-7 (2016).
  - [12] Yonggang, G. Y., Zhang, X., Zunger, A. Natural off-stoichiometry causes carrier doping in half-Heusler filled tetrahedral structures. *Phys. Rev. B* **95**, 085201 (2017).
  - [13] Patel, S. J., et al. Surface and electronic structure of epitaxial PtLuSb (001) thin film. *Appl. Phys. Lett.* **104**, 201603 (2014).
  - [14] Supplementary Information
  - [15] Linder, J., Yokoyama, T., Sudbø, A. Anomalous finite size effects on surface states in the topological insulator Bi<sub>2</sub>Se<sub>3</sub>. *Phys. Rev. B* **80**, 205401 (2009).
  - [16] Brillson, L. J., Surfaces and interfaces of electronic materials *John Wiley and Sons* (2010).
  - [17] Ando, Y., Topological insulator materials *J. Phys. Soc. Jpn.* **82**, 102001 (2003).
  - [18] Volkov, B. A., Pankratov, O. Two-dimensional massless electrons in an inverted contact *JETP Lett.* **42**, 178 (1985).
  - [19] Tchoumakov, S., et al. Volkov-Pankratov states in topological heterojunctions. *Phys. Rev. B* **96**, 201302 (2017).
  - [20] Inhofer, A., et al. Observation of Volkov-Pankratov states in topological HgTe heterojunctions using high-frequency

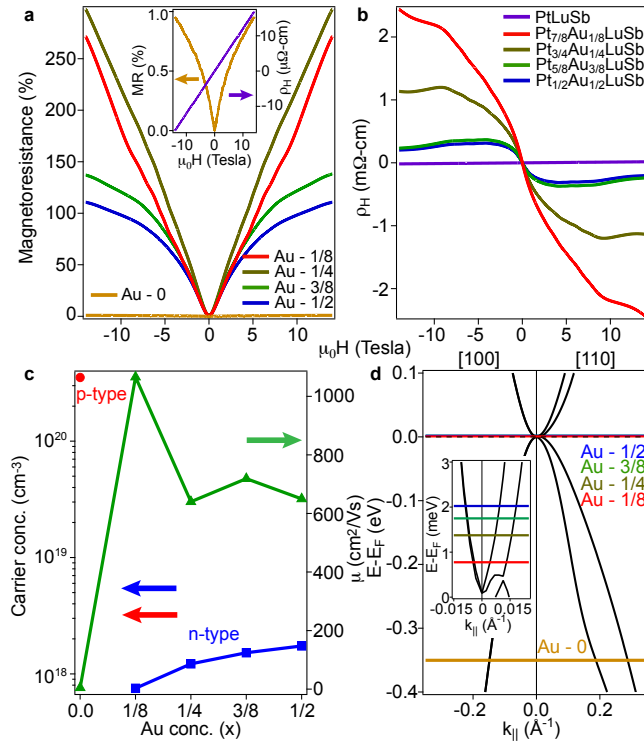


Figure 1: **Transport properties of Pt<sub>1-x</sub>Au<sub>x</sub>LuSb thin films** **a.** Magnetoconductance and **b.** Hall resistance as a function of Au concentration in Pt<sub>1-x</sub>Au<sub>x</sub>LuSb thin films. Inset in **a** shows the magnetoconductance and Hall resistance of PtLuSb. **c.** Carrier concentration and mobility as a function of Au concentration in Pt<sub>1-x</sub>Au<sub>x</sub>LuSb, estimated from the Hall coefficient. **d.** Position of the Fermi level as a function of Au concentration.

compressibility. *Phys. Rev. B* **96**, 195104 (2017).

- [21] Armitage, N. P., Mele, E. J., Vishwanath, A., Weyl and Dirac semimetals in three-dimensional solids. *Rev. Mod. Phys.* **90**, 015001 (2018).
- [22] Cano, J., et al. Chiral anomaly factory: Creating Weyl fermions with a magnetic field. *Phys. Rev. B* **95**, 161306 (2017).
- [23] Kresse, G., Furthmüller, J. Efficiency of ab-initio total energy calculations for metals and semiconductors using a plane-wave basis set. *Comput. Mater. Sci.* **6**, 15-50 (1996).
- [24] Perdew, J. P., Burke, K., Ernzerhof, M. Generalized Gradient Approximation Made Simple. *Phys. Rev. Lett.* **77**, 3865-3868 (1996).
- [25] Monkhorst, H. J., Pack, J. D., Special points for Brillouin-zone integrations. *Phys. Rev. B* **13**, 5188-5192 (1976).
- [26] Blöchl, P. E., Projector augmented-wave method. *Phys. Rev. B* **50**, 17953-17979 (1994).

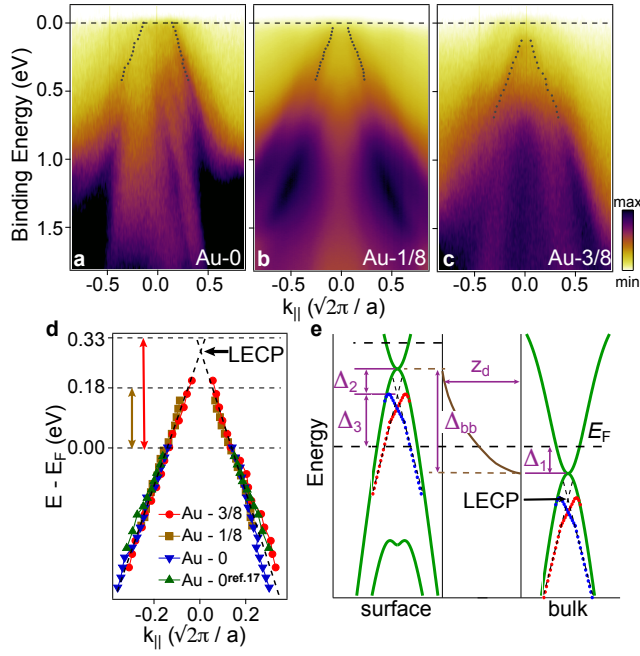


Figure 2: **Topological surface state (TSS) in  $\text{Pt}_{1-x}\text{Au}_x\text{LuSb}$  thin films** ARPES measurements along  $\bar{\Gamma} - \bar{X}$  in  $\text{Pt}_{1-x}\text{Au}_x\text{LuSb}$  thin films close to the bulk  $\Gamma$  point for **a.**  $x=0$  **b.**  $x=1/8$  **c.**  $x=3/8$ . **d.** Extracted dispersion of the topological surface state (TSS) showing the shift in chemical potential with the addition of gold (Au). **e.** Schematic of upward band-bending observed in  $\text{Pt}_{1-x}\text{Au}_x\text{LuSb}$  thin films.  $\Delta_1$ ,  $\Delta_2$ , and  $\Delta_3$  represents position of the Fermi level with respect to  $\Gamma_8$  in the bulk, position of the linear extrapolated crossing point (LECP) with respect to  $\Gamma_8$ , and position of the linear extrapolated crossing point with respect to the Fermi level at the surface, which are estimated from Hall measurements along with bulk DFT calculations, DFT slab calculations, and ARPES measurements, respectively. Band bending ( $\Delta_{bb}$ ) is obtained as  $\Delta_{bb} = \Delta_1 + \Delta_2 + \Delta_3$ . Details about the estimation of band bending can be found in the Supplementary Information [14]

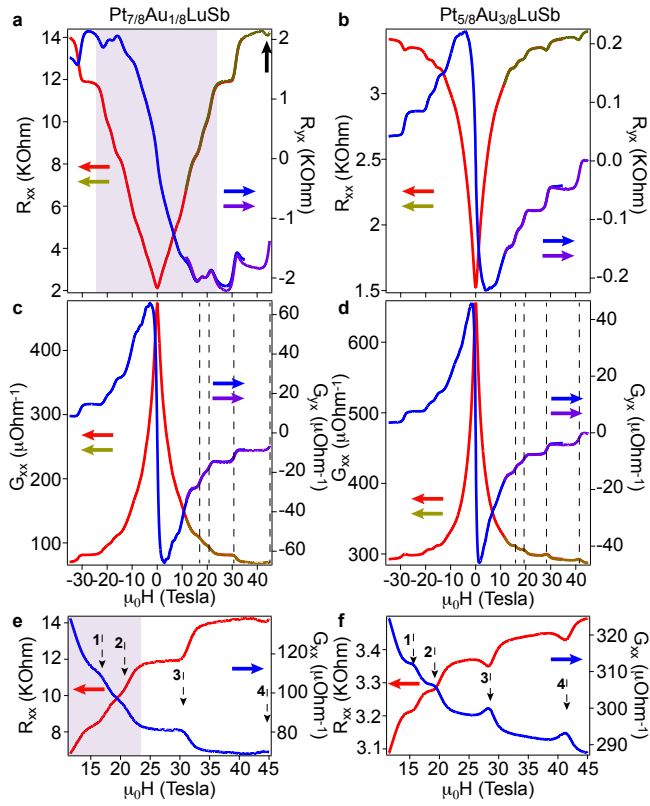


Figure 3: **Linear magnetoresistance in topological semi-metallic thin films.** Longitudinal and Hall resistance in **a.**  $\text{Pt}_{7/8}\text{Au}_{1/8}\text{LuSb}$  and **b.**  $\text{Pt}_{5/8}\text{Au}_{3/8}\text{LuSb}$ . Longitudinal and Hall conductance in **c.**  $\text{Pt}_{7/8}\text{Au}_{1/8}\text{LuSb}$  and **d.**  $\text{Pt}_{5/8}\text{Au}_{3/8}\text{LuSb}$ . Correspondence between local minima in longitudinal resistance and local maxima in longitudinal conductance in **e.**  $\text{Pt}_{7/8}\text{Au}_{1/8}\text{LuSb}$  and **f.**  $\text{Pt}_{5/8}\text{Au}_{3/8}\text{LuSb}$ . Linear magnetoresistance behavior in  $\text{Pt}_{7/8}\text{Au}_{1/8}\text{LuSb}$  is highlighted by a light violet background in **a** and **e**.

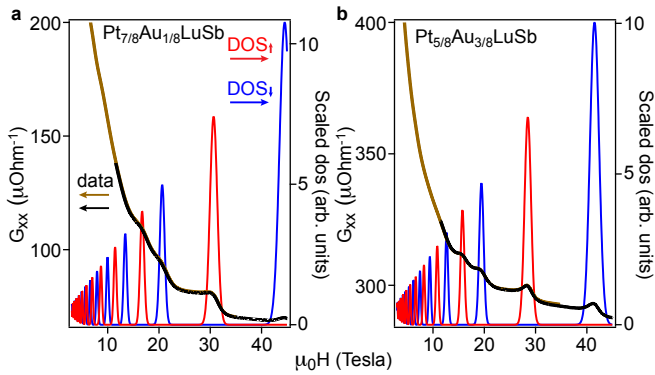


Figure 4: **Fits to the quantum Hall data in  $\text{Pt}_{1-x}\text{Au}_x\text{LuSb}$**  Conductivity and corresponding fits to the *two-Dirac model*, as described in the text, for **a.**  $\text{Pt}_{7/8}\text{Au}_{1/8}\text{LuSb}$  and **b.**  $\text{Pt}_{5/8}\text{Au}_{3/8}\text{LuSb}$ .  $\text{DOS}_\uparrow$  and  $\text{DOS}_\downarrow$  are the contributions from the Zeeman split Landau levels with spin direction along and opposite to the applied magnetic field, respectively.